

Microstructure and microtexture of highly cold-rolled commercially pure titanium

N. Bozzolo · N. Dewobroto · H. R. Wenk ·
F. Wagner

Received: 15 June 2005 / Accepted: 26 January 2006 / Published online: 22 December 2006
© Springer Science+Business Media, LLC 2006

Abstract The microstructure and texture evolution of a commercially pure titanium sheet during cold-rolling is investigated in detail by X-ray diffraction and by orientation imaging in the FEG-SEM and in the TEM. The experimental data are compared with simulation results obtained by a viscoplastic self-consistent model. The aim of this work is to provide with a detailed description of the fine scale deformation structures obtained after 80% cold-rolling and to identify the mechanisms by which these structures form. Such a detailed investigation is nowadays possible thanks to high spatial resolution orientation imaging techniques. This work highlights the important role of mechanical twinning as one of the grain fragmentation mechanisms. The microstructure obtained after 80% thickness reduction can be separated into two distinct parts: 85 vol.% of the material is fine-subdivided with highly misoriented sub-micron features and the others 15 vol.% consist in lamellar structures formed in grains initially oriented in a particular region of orientation

space, which have not undergone twinning. The influence of these structures on recrystallization mechanisms are also discussed.

Introduction

Titanium is an important structural metal for high performance applications. The preferred orientations of crystals have an important effect on physical and mechanical properties [1, 2] and need to be optimized. Texture develops during deformation and is modified by subsequent recrystallization and grain growth. Deformation mechanisms are slip and mechanical twinning. They have been studied both on single crystals and on polycrystalline samples [e.g. 3–5] and those mechanisms have been used as a basis for modeling deformation [e.g. 6–8]. Systematic texture changes also occur during recrystallization and grain growth [9–13], but not much is known about the way recrystallization proceeds.

The detailed description of microstructures and local textures in heavily deformed materials may help in a better understanding of the deformation mechanisms and their relationship to mechanisms during the initiation of recrystallization. The recent development of techniques for local orientation measurements, such as electron backscatter diffraction (EBSD) coupled to field emission gun scanning electron microscopy (FEG-SEM) and indexing of Kossel/Kikuchi patterns obtained by transmission electron microscopy (TEM), have made such investigations feasible. These techniques indeed provide a spatial resolution suited to the

N. Bozzolo (✉) · N. Dewobroto · F. Wagner
Laboratoire d'Etude des Textures et Application aux
Matériaux (LETAM – UMR CNRS 7078), Université Paul
Verlaine-Metz, Ile du Saulcy, Metz cedex 01 57045, France
e-mail: nathalie.bozzolo@univ-metz.fr

Present Address:

N. Dewobroto
Swissmetal Dornach, Weidenstrasse 50, 4143 Dornach 1,
Switzerland

H. R. Wenk
Department of Earth and Planetary Science, University of
California, Berkeley, CA 94720-4767, USA

very fine scale at which the deformation structures develop. In this paper, they are used to characterize the texture and microstructure evolution of α -Ti (hcp) during cold-rolling down to 80% thickness reduction. The experimental data are interpreted in combination with the results of numerical simulations of the deformation process with the aim to describe the mechanisms by which the heterogeneity of the deformation structures is formed.

Experimental procedures

The starting material is a 3 mm thick sheet of commercially pure titanium (Ti grade 2 within the ASTM standards) in a fully recrystallized state and containing the following impurities (in weight ppm): C 52, Fe 237, H 3, N 41, O 1062 and Si < 100. Cold-rolling is performed down to 80% thickness reduction in 3% steps.

For XRD texture analysis, about one third of the thickness was removed by mechanical polishing in order to exclude surface artifacts. Five incomplete pole figures ((10–10), (0002), (10–11), (10–12) and (10–13)) were measured by XRD in reflection geometry with Co-K α radiation and from those the orientation distribution function (ODF) was calculated with the harmonic method, using an expansion to $L_{\max} = 32$, applying a ghost correction [14, 15] and imposing the orthorhombic sample symmetry.

Cross-sections were prepared from the same samples used for X-ray pole figure measurements. They were mechanically and further electrolytically polished (with a 10% HClO₄–90% CH₃OH solution, under 17V at 6 °C) in order to achieve a surface quality required for EBSD measurements. These samples were analyzed with a Jeol 6500F FEG-SEM operating at 15 kV, and equipped with an EBSD orientation imaging system. The Kikuchi patterns were acquired with a ultra-sensitive CCD camera and processed with the Channel 5 software from HKL technologies.

Thin foils were prepared for TEM characterization in the rolling plane RD–TD or in the longitudinal section TD–ND (with RD ND TD respectively rolling, normal and transverse directions). The thin foil preparation consisted in two steps: first mechanical polishing to reduce the thickness to 50 μ m and then either electrolytic thinning or argon ion-milling down to electron transparency. The TEM investigations were performed with a CM200 Philips microscope operating at 200 kV accelerating voltage and equipped with a Gatan CCD camera for image and diffraction pattern acquisition. Orientation measurements were done by

indexing Kossel/Kikuchi patterns, using the Euclid's Phantasies software [16]. With this method, the precision for misorientations between different data points of the same thin foil is close to 0.1°. The absolute accuracy of orientation measurements within the macroscopic RD–TD–ND system is considerably lower because of the manual operations of sample positioning in the saw, polishing and positioning in the TEM sample holder. The spatial resolution is almost equal to the size of the beam when focussed on the sample, i.e. 20 nm for the measurements reported here.

When dealing with texture components, it is very convenient to describe the crystal orientation by a set of three Euler angles. The ones used here correspond to the definition given by Bunge [17] with the crystal coordinate system defined as $\{X = [10\bar{1}0], Y = [\bar{1}2\bar{1}0], Z = [0001]\}$.

Method for the simulation of deformation

The Visco-Plastic Self-Consistent method based on the tangent approach [18] as implemented in the VPSC5 computer program [19] was used in this work to simulate the texture evolution. Results basically agree with previous work [20–23]. In this context our principal interest has been in obtaining rotation trajectories of individual orientations to compare with experimentally observed orientation gradients and to investigate activity of deformation systems in differently oriented grains. The self-consistent approach regards each grain as an inclusion embedded in a homogeneous equivalent medium, having the average properties of the polycrystal. Equilibrium and compatibility are maintained in the average over the whole polycrystal, but not locally. Some grains may deform a lot and others very little.

For materials that are subject to mechanical twinning, this mechanism is critical since it introduces large orientation changes. In the VPSC5 program, twinning is treated as a slip system with a critical shear stress but with additional twin reorientation. Twinning basically creates new orientations, which is inconvenient for simulations. In order to keep the number of orientations constant, the program applies a method proposed by Van Houtte [24] and further refined by Tomé et al. [20]. This method uses a probability criterion as well as the deformation rate on the twin system to statistically determine if a given grain twins during a certain step. Either a grain twins completely and the old orientation vanishes, or it does not twin and the old orientation is kept.

As starting texture we used a set of orientations modeled after the initial texture, discretized into

$5 \times 5 \times 5^\circ$ cells in the Euler space. For starting orientations of the simulations, we picked the 2000 ODF cells with the highest orientation densities and weighted each orientation with density and representative cell volume. The output of the simulation program includes the list of the 2000 new orientations after 0.29, 0.58 and 0.87 effective strain, which can be further processed by the harmonic method for producing a continuous ODF from which pole figures can be recalculated.

We tried several combinations of critical shear stresses for slip/twinning systems and hardening laws. In the end we selected a set that reasonably reproduces the experimental texture components. Critical shear stresses (given in Table 1) emphasize prismatic slip and twinning. Pyramidal and basal slips were allowed but did not get significantly activated. For strain rate

sensitivity we chose a value of 0.05 (stress exponent 19). We selected a linear hardening law in which shear stresses were more or less doubled after a strain of 1.0.

Results

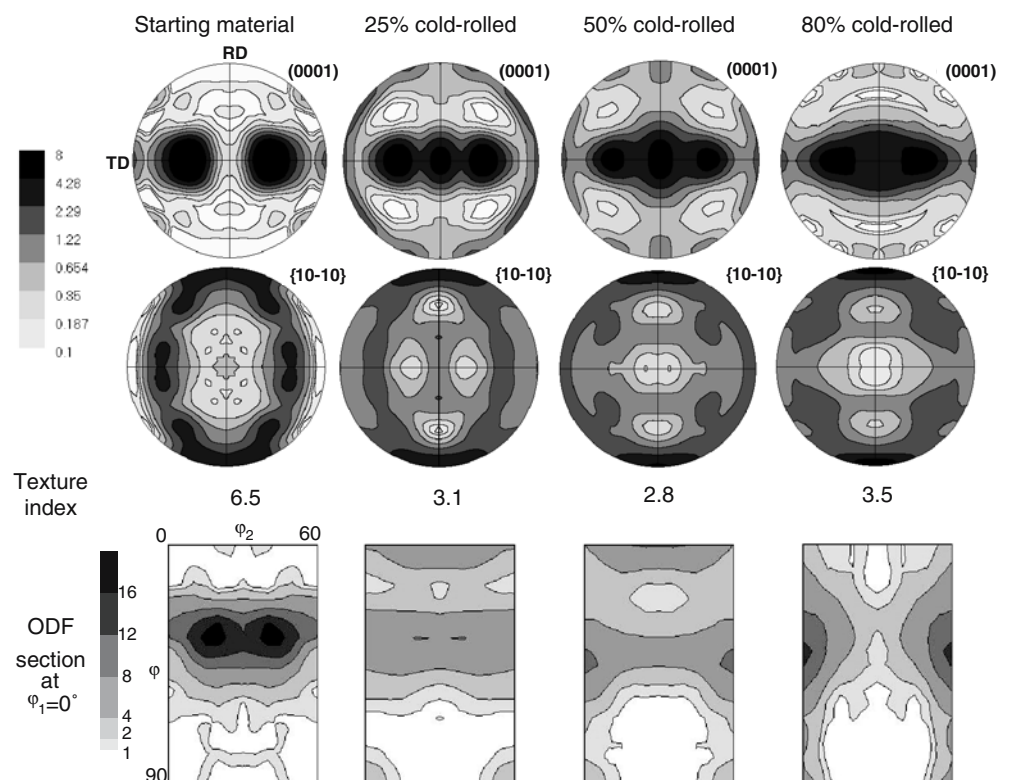
Experimental bulk texture evolution during cold-rolling

Figure 1 shows the experimentally measured texture evolution starting from the fully recrystallized state to the 80% cold-rolled one. The textures are represented in (0001) and {10–10} pole figures and also in the $\varphi_1 = 0$ section of the ODF, that contain most of the relevant orientation information in the context of this paper. The starting material (first column of Fig. 1) has a

Table 1 Slip and twinning systems assumed in simulations

			Critical resolved shear stress	Hardening parameter
Slip systems	Prismatic	$\{10\text{--}10\}\langle\text{--}12\text{--}10\rangle$	0.85	$h = 1$
	Basal	$\{0001\}\langle\text{--}12\text{--}10\rangle$	2.5	$h = 5$
	Pyramidal $c + a$	$\{10\text{--}11\}\langle\text{--}1\text{--}123\rangle$	2.5	$h = 4$
Twin systems	Tensile ($\gamma = 0.163$)	$\{10\text{--}12\}\langle\text{--}1011\rangle$	1.2	$h = 1$
	Compressive ($\gamma = 0.225$)	$\{2\text{--}1\text{--}12\}\langle 2\text{--}1\text{--}1\text{--}3\rangle$	1.7	$h = 3$
Stress exponent: 19				

Fig. 1 Texture evolution during deformation (XRD data processed by the harmonic method)—Recalculated pole figures (equal area projection), texture index values and ODF section at $\varphi_1 = 0^\circ$ for the initial material and after 25%, 50% and 80% thickness reduction



texture with (0001) maxima inclined 35° from ND towards \pm TD. The $\{10\text{--}10\}$ pole figures show intensities distributed on girdles at 90° from the (0001) maxima. This texture, characterized by an ODF maximum around $\{\varphi_1 = 0^\circ, \varphi = 35^\circ, \varphi_2 = 15\text{--}20^\circ\}$, is typical of recrystallized titanium having undergone moderate grain growth [25]. It is intermediate between the texture at the end of primary recrystallization (for which the component A $\{\varphi_1 = 0^\circ, \Phi = 40^\circ, \varphi_2 = 0^\circ\}$, displayed schematically in Fig. 2, is the main component), and the texture after advanced grain growth (with component B $\{\varphi_1 = 0^\circ, \Phi = 30^\circ, \varphi_2 = 30^\circ\}$ as main one, see also Fig. 2). The texture index is 6.5, indicative of a rather strong texture. Note that the terminology of “texture component” is used here to describe wide ODF peaks centered on given orientations.

During cold-rolling the texture weakens, the (0001) maxima become spread out, and the $\{10\text{--}10\}$ maximum shifts towards the rolling direction and becomes a very distinct texture feature at 80%. After 80% cold-rolling the (0001) maximum is at 40° between ND and TD, with considerable spread (ODF component A $\{\varphi_1 = 0^\circ, \Phi = 40^\circ, \varphi_2 = 0^\circ\}$, Fig. 2). The texture index is reduced to 3.5. During cold-rolling the texture strength first decreases rapidly, already after 25% thickness reduction and then remains fairly stable. At intermediate strains (25% and 50% thickness reduction, respectively second and third columns in Fig. 1), secondary components develop with $[0001]$ axes close to the normal direction (component C $\{\varphi_1 = 0^\circ, \Phi = 0^\circ, \varphi_2 = 30^\circ\}$) and with $[0001]$ axes perpendicular to the normal direction (component D at $\{\varphi_1 = 0^\circ, \Phi = 90^\circ, \varphi_2 = 0^\circ\}$). The

component C disappears again at larger strains while component D remains until 80% thickness reduction.

Simulation of the bulk texture evolution during deformation

Simulated bulk textures for 0.29, 0.58 and 0.87 effective strain are shown on Fig. 3a and b. Figure 3c shows the relative activity of the different deformation systems. Prismatic slip is by far the most active one. Basal and pyramidal slip are barely activated. Compressive and tensile twinning operate during the whole deformation path, with a higher activity of compressive twinning at the beginning where the activity of tensile twinning is reduced. The mean number of active systems at each deformation step is close to 3, and does not vary much during the deformation path.

The main texture component (Component A) obtained after 80% cold-rolling is reproduced. Moreover, the secondary texture component C, which develops at intermediate strains and disappears again at higher strain, is also visible in the simulations. The secondary component at D is weaker in the simulated texture and only visible at 0.29 effective strain. The simulation results are in agreement with the experimental data with regards to the nature of the appearing components but they do nevertheless show also some discrepancy. At 0.29 strain which corresponds to 22% thickness reduction, component A is too much developed and slightly shifted to higher Φ values. Components C and D disappear too fast, they do not exist any longer in the simulated textures after 0.87 strain

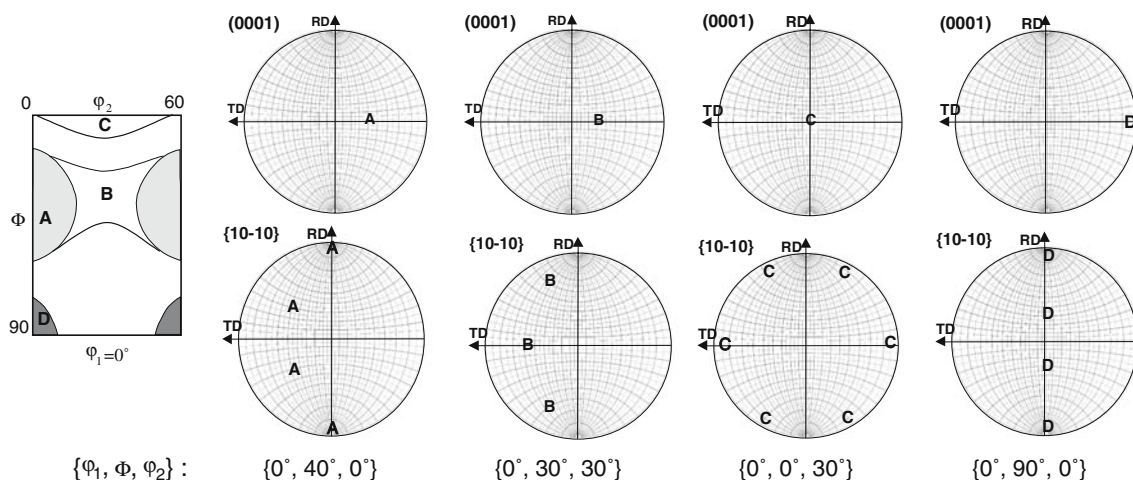


Fig. 2 Schematic ODF section at $\varphi_1 = 0^\circ$ and (0001) and $\{10\text{--}10\}$ pole figures defining the different components constituting the textures of titanium (stereographic projection). Component A is the main one after 80% cold-rolling and still after recrystallization; Component B becomes the main one after extended grain

growth; Component C develops at 25% thickness reduction and disappears again at larger strains; Component D develops during cold-rolling and remains until 80% thickness reduction. These components have sample-symmetry equivalents which are not displayed here

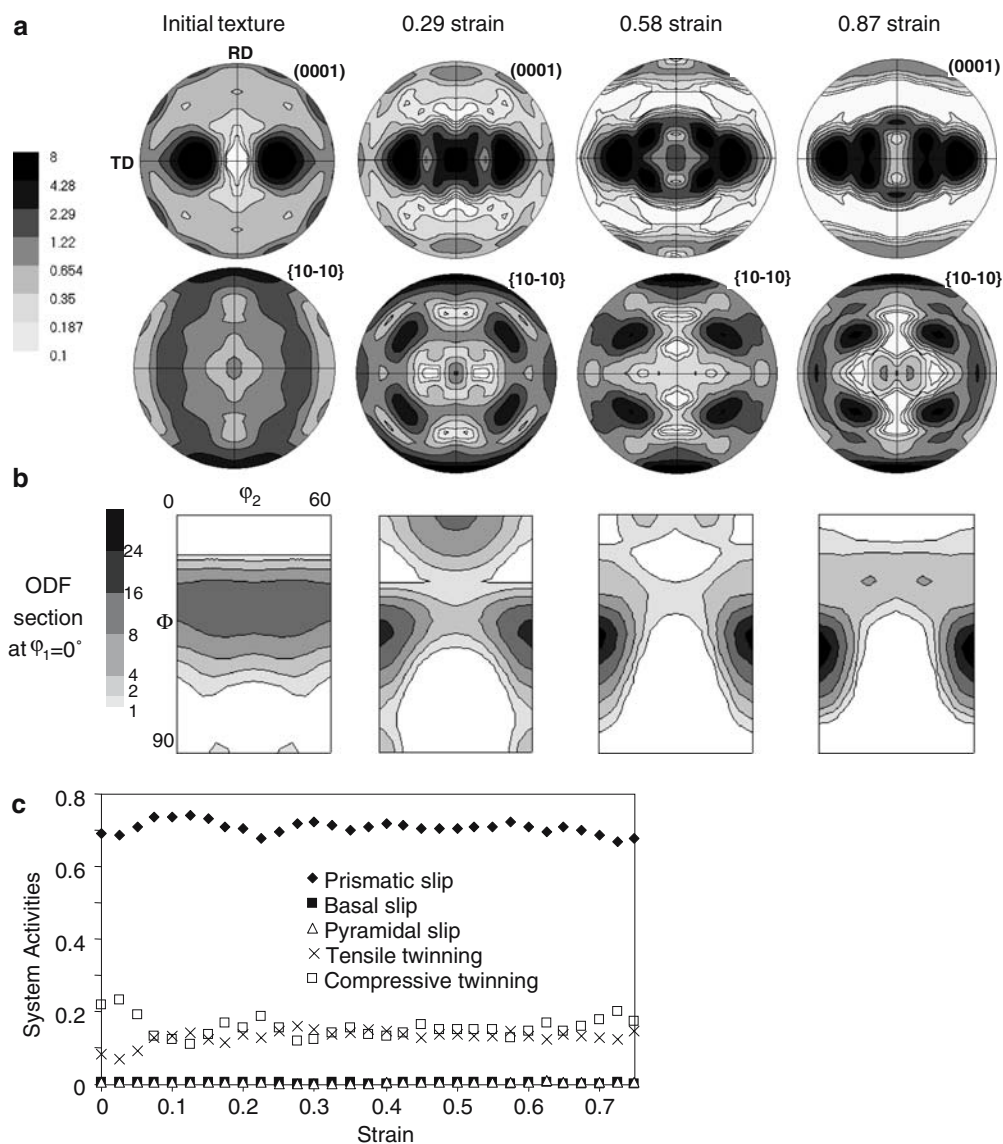


Fig. 3 VPSC simulation of the cold-rolling texture evolution. Initial texture and VPSC simulations processed with harmonic method after 0.29, 0.58 and 0.87 effective strain represented with

(a) (0001) and {10–10} pole figures (equal area projections) and (b) ODF section at $\phi_1 = 0^\circ$. (c) Activity of slip and twinning systems

(corresponding to 53% thickness reduction). Several reasons can be evoked for this discrepancy: (i) both the relative critical shear stresses of the different slip systems and the hardening laws are far from being unambiguously determined in HCP metals. (ii) twinning is treated similarly to a slip system and the model does not allow grain fragmentation, which is probably a major drawback when the grain fragmentation is one of the main mechanisms for microstructure evolution, which is the case here as will be demonstrated below. (iii) only the 2000 $5 \times 5 \times 5^\circ$ ODF cells with highest weights have been processed due to a limitation of the simulation computer program; the orientations with low weights may contribute to strengthen minor

components. The numerical simulation results, even if they are not in perfect agreement with the experimental data, will be nevertheless helpful to understand and explain the microstructure evolution.

Microstructure evolution upon cold-rolling characterized by EBSD

The microstructure of the initial sheet, shown in Fig. 4a, is equiaxed with a mean grain size of 30 μm . After 25% cold-rolling (Fig. 4b), some of the initial grains show twin lamellae, which have been identified by EBSD and based on their orientation as being either compressive or tensile twins. A higher occurrence was

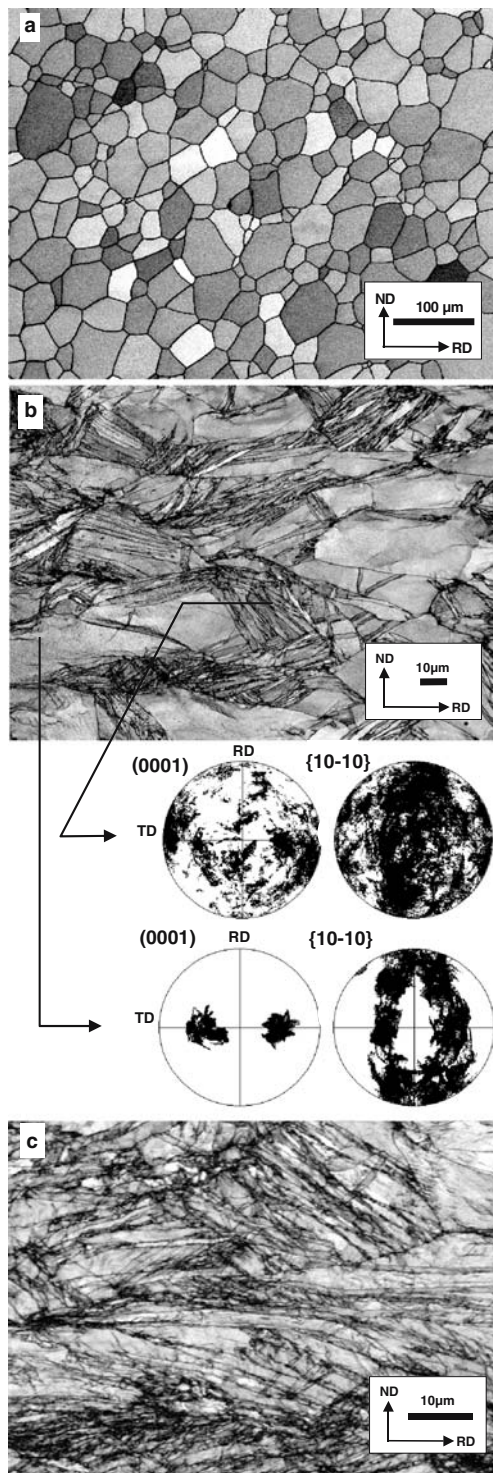


Fig. 4 Microstructure evolution upon cold-rolling (as revealed by EBSD band contrast maps in the longitudinal plane). **(a)** starting material: equiaxed grained with a mean grain size around 30 μm. **(b)** after 25% cold-rolling and orientations measured in the twinned and in the untwinned areas represented in (0001) and {10-10} pole figures (stereographic projection). **(c)** after 50% cold-rolling

observed for compressive twins ($\{11-22\}\langle 11-2-3\rangle$). The $\{10-12\}\langle 10-1-1\rangle$ tensile twins were about half as frequent and $\{11-21\}\langle 11-2-6\rangle$ tensile twins were only rarely observed. The analysis of the EBSD maps showed that multiple twinning occurred also, with often tensile twins appearing in compressive ones. Some other areas have not undergone twinning. Figure 4b also shows the orientations measured by EBSD in the twinned and the untwinned areas in (0001) and {10-10} pole figures. Twinning generates many different orientations, “randomizing the global texture”, and is probably responsible for the fast decrease of the texture index at the beginning of deformation, as already suggested in earlier work [11, 26]. In particular, it is obviously responsible for the appearance of the $\{\varphi_1 = 0^\circ, \Phi = 0^\circ, \varphi_2 = 30^\circ\}$ and $\{\varphi_1 = 0^\circ, \Phi = 90^\circ, \varphi_2 = 0^\circ\}$ secondary texture components (C and D) with $\langle 0001\rangle$ axes close to the normal and transverse directions, respectively. With increasing strain (50% thickness reduction shown in Fig. 4c), the twinned areas are subdivided into smaller and smaller features. The twin orientation relationships are lost due to additional slip activity in and around the twin lamellae and to the accumulation of dislocations in the twin boundaries.

After cold-rolling to a reduction of 80% (Fig. 5), the microstructure changes and becomes very fine-grained, except for some areas which include lamellar substructures elongated along the RD. These lamellar areas correspond to the initial grains which deformed only by slip, without twinning. The lamellar areas account for about 15 vol. % of the material. The other 85% are subdivided into very small and highly misoriented features. Shear bands, with characteristic bending of the deformation structures on both sides, are also formed in this part of the material as visible in Fig. 5a. The pole figures of Fig. 5b show the orientations measured in the few μm^2 wide areas marked A, B and C. A is in a shear band and shows a wide spread of orientations. B is constituted by subdivided material outside the shear band and displays an almost equal wide orientation spread. By contrast, area C selected in a lamella shows a narrow orientation range, with [0001] axes at about 50° from ND and slightly tilting in the ND-TD plane and with {10-10} poles rotating around [0001] axes within a $\sim 30^\circ$ wide sector. The misorientation profiles of Fig. 5c and d, respectively across a set of lamellae and along one lamella show that lamellae are highly misoriented (several tens of degrees), and that the misorientation is very much lower along the lamellae (in the 1° range). The next paragraph is dedicated to a more detailed

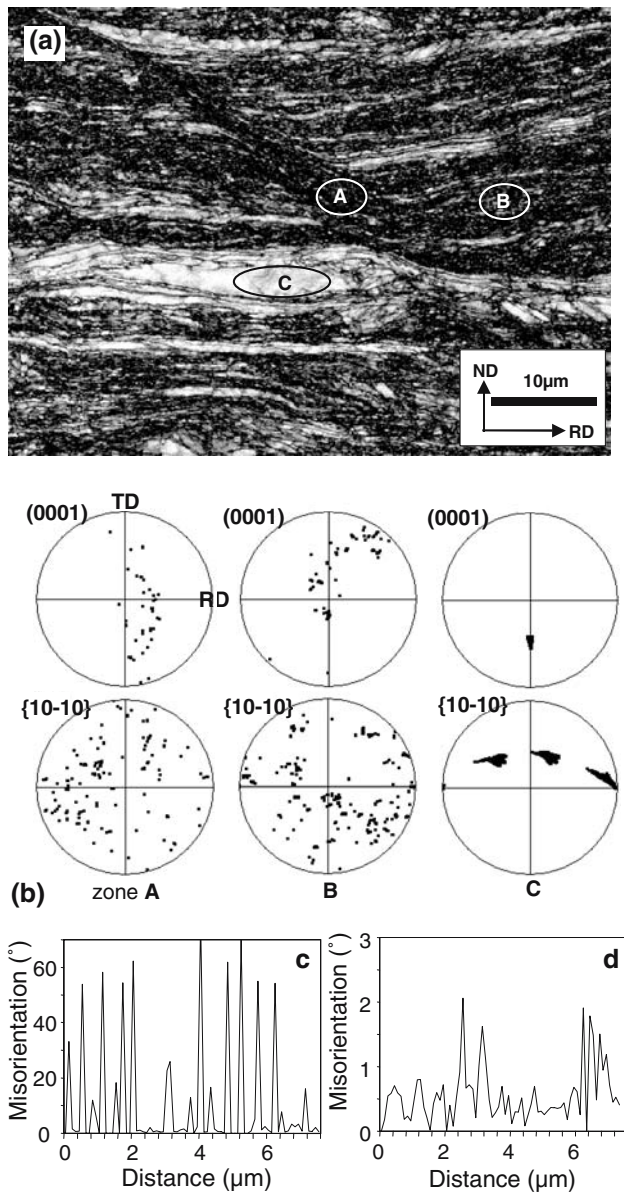


Fig. 5 (a) Microstructure of the 80% cold-rolled sheet (as revealed by EBSD band contrast map in the longitudinal plane). (b) Orientations measured in areas A, B and C displayed on (0001) and {10–10} pole figures (stereographic projection). (c–d) Misorientation profiles in an area of type C: across the lamellae (c) and along one lamella (d)

characterization work concerning these features observed in the 80% cold-rolled microstructure.

Detailed characterization of the microstructure local features in the 80% cold-rolled material with the TEM

The 80% cold-rolled microstructure is constituted by two types of local structures: lamellar areas coming from the initial grains which did not twin during

deformation and fine-subdivided material which accounts for 85 vol.%. TEM was used to further characterize these two types of deformation structures.

Figure 6a shows a bright field TEM image of one of the lamellae formed in the untwinned areas. This image is taken in the rolling plane, perpendicular to the previous view of Fig. 5. By using Kossel/Kikuchi diffraction pattern indexing, orientations could be measured along a line parallel to the RD (continuous line) and along a line parallel to the TD (dashed line). These orientation data are represented on Fig. 6b and c in (0001) and {10–10} pole figures. The orientations along RD (Fig. 6b) are very similar to those of Fig. 5c obtained by EBSD in the longitudinal plane, with <0001> axes in a constant position and {10–10} poles rotating around [0001]. Along TD, the situation is “inverted”, [0001] axes rotate around the {10–10} pole which is parallel to RD. The misorientation profile along TD (in grey on Fig. 6d) shows a fairly regular orientation gradient of about $4^\circ\mu\text{m}^{-1}$. The local misorientations are quite small but the misorientation reaches 40° over the whole width of the lamella. Along a line parallel to the RD, the orientation is quite stable in the middle of the lamella, consistently with the plateau observed in the central part of the misorientation angle profile (in black on Fig. 6d), but near the boundaries of the lamella, much stronger orientation gradients are observed, as a result of the interaction with the neighboring severely deformed material.

The very fine subdivided material could also be characterized by TEM (Figs. 7 and 8). According to the sample section in which the thin foil is prepared, the microstructural details are more or less visible. Figure 7a shows a typical bright field image in the rolling plane. The contrast is extremely disturbed with many Moiré fringes, details at the 100 nm range in size can be distinguished. The SAED pattern taken in this area, corresponding to only $1\ \mu\text{m}^2$, looks more like a ring pattern than like a single-crystal pattern, showing that this very small material volume is constituted by many fragments of very different orientations. Correspondingly pole figures (Fig.7c) show how widely scattered the local orientations can be in such an area that is only $1\ \mu\text{m}^2$ wide. One should mention that in fine-subdivided areas, it is not possible to record indexable patterns at all locations. Kossel/Kikuchi patterns are usually very diffuse, except in some places where enough bands can be distinguished to index the pattern and get the orientation. Strong contrasts in the bright field images do not always correspond to high misorientations, it is therefore very dangerous to interpret the TEM contrast without considering the orientation information.

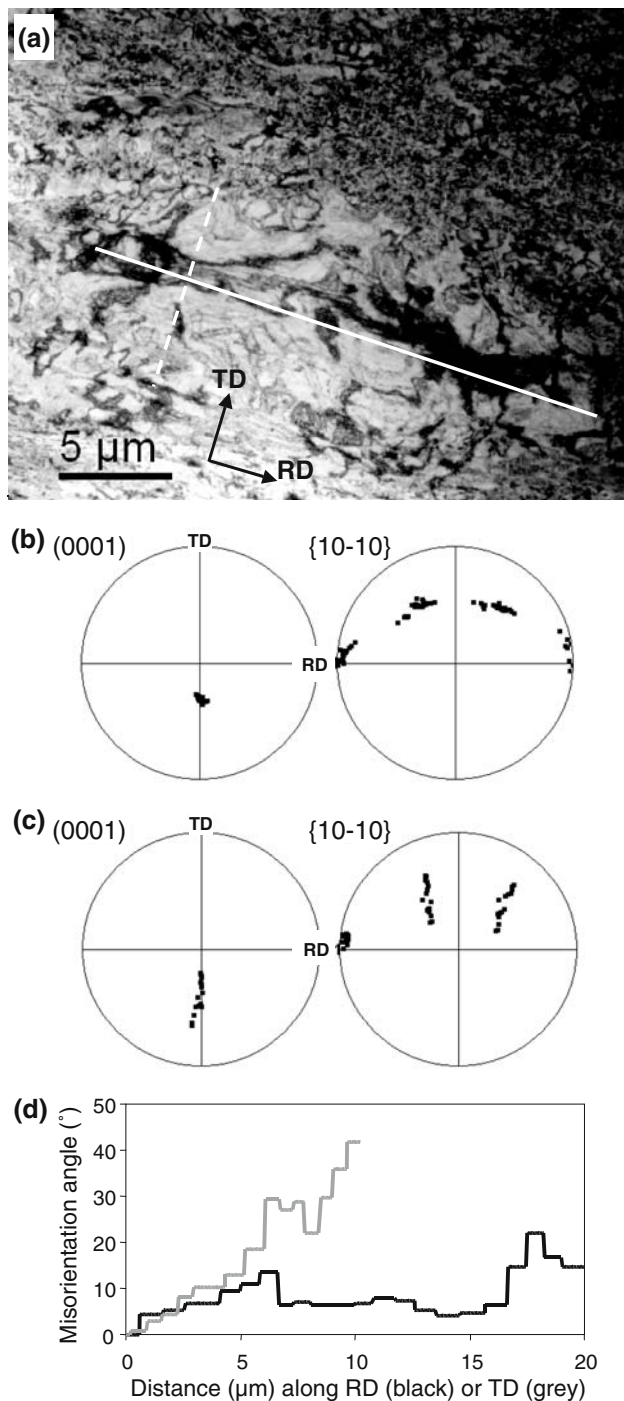


Fig. 6 TEM characterization of a lamella constituting the untwinned areas (type C in Fig. 5). **(a)** Bright field image in the rolling plane. **(b)** Local orientations measured along RD (white line) and **(c)** along TD (dashed line) in the lamella (pole figures in stereographic projection). **(d)** Misorientation profiles along RD and along TD (The misorientation angle is calculated for each data point with the first point of the measurement line)

The TEM bright field image of Fig. 8a was taken in the transverse plane (electron beam parallel to the transverse direction). In this section, the structures

appear much more clearly than in the rolling plane, with thin elongated domains along the rolling direction. In this area most of the Kossel/Kikuchi patterns were indexable (except in some parts which were either too thin or convoluted by overlapping parts of different orientation). In such regions, orientation maps could be acquired automatically. The one of Fig. 8 is about $4 \mu\text{m}^2$ and includes very different orientations, as visible on the pole figures. In agreement with the global texture, these measurements made at a very small scale do show a concentration of $\{10\text{--}10\}$ poles near RD. High misorientations can be found along the boundaries of the elongated features. Inside the elongated features misorientations are much lower. This situation shows some similarities with the lamellar structured areas of Fig. 5, but on a smaller scale. Here again, the orientation information is much richer than the simple bright field contrast.

Discussion

Initially equiaxed, the microstructure of this commercially pure titanium sheet develops very heterogeneous structures upon cold-rolling. According to the initial orientation of the grains, different deformation mechanisms take place locally. Twinning occurs at the beginning of deformation in most of the grains (about 85 vol.%). These grains are subdivided into increasingly smaller and highly misoriented features. In this part of the material, shear bands also form. Shear bands show a wide spread of orientations and high misorientations at a low scale. In terms of local misorientations, the shear bands are nevertheless not significantly more disturbed than the rest of the 85% subdivided part of the material. The complementary part (15 vol.%) is constituted by grains which are not favorably oriented for twinning and deform only by slip. These elongated areas had already been observed in the past and associated with the absence of twinning [27] but their internal structure had not been investigated. In these areas, lamellar structures form. The lamellae are characterized by very low local misorientations inside and much higher misorientations between them. Inside a single lamella, the orientation changes gradually and in a different manner depending on the direction along which the orientation gradient is measured. Along RD, the misorientation makes the $\{10\text{--}10\}$ poles rotate around the $[0001]$ axis. Along TD, $[0001]$ axes tilt around the $\{10\text{--}10\}$ poles which are parallel to RD. These grains which deform without twinning have $[0001]$ axes tilted by about 50° from ND to \pm TD.

Fig. 7 (a) TEM bright field images of the subdivided part of the 80% rolled microstructure (Rolling plane). (b) SAED pattern corresponding to $1 \mu\text{m}^2$. (c) local orientations measured within a $1 \mu\text{m}^2$ area (stereographic projection)

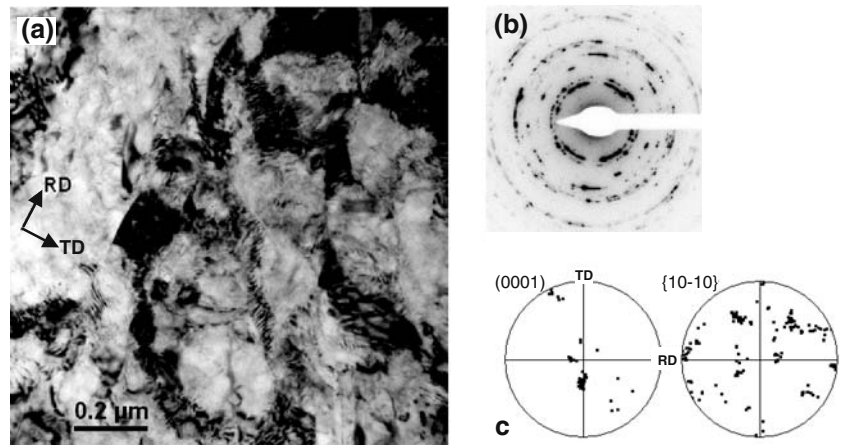
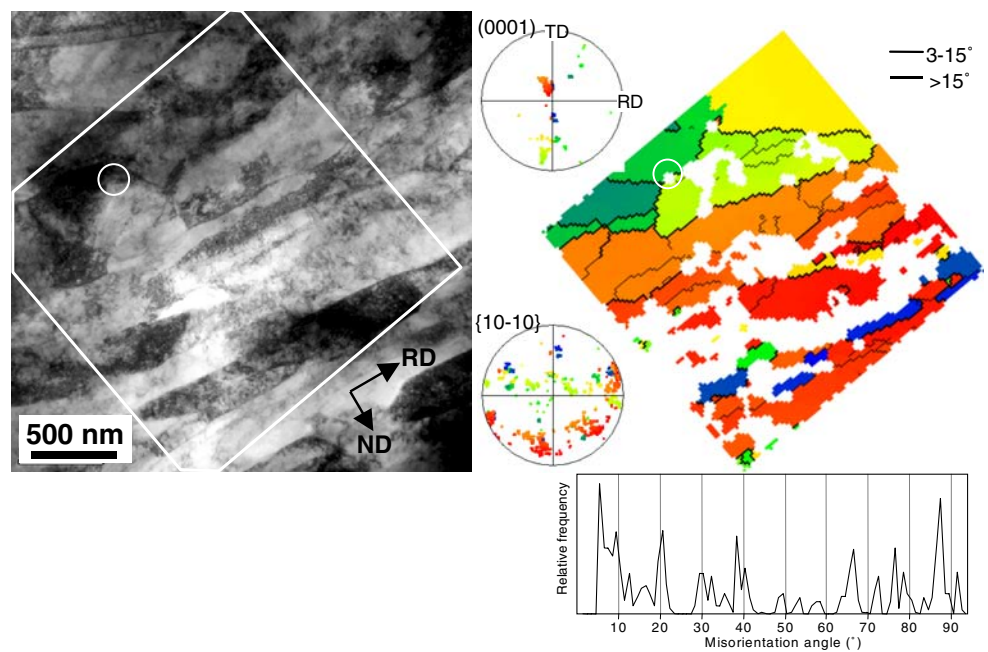


Fig. 8 Bright field image of the subdivided part of the 80% rolled microstructure (cross-section in the longitudinal plane), corresponding TEM orientation map and pole figures (stereographic projection) and distribution of misorientation angles ($>5^\circ$) between neighboring pixels. (The white circle gives a landmark; white pixels correspond to non-indexed patterns)

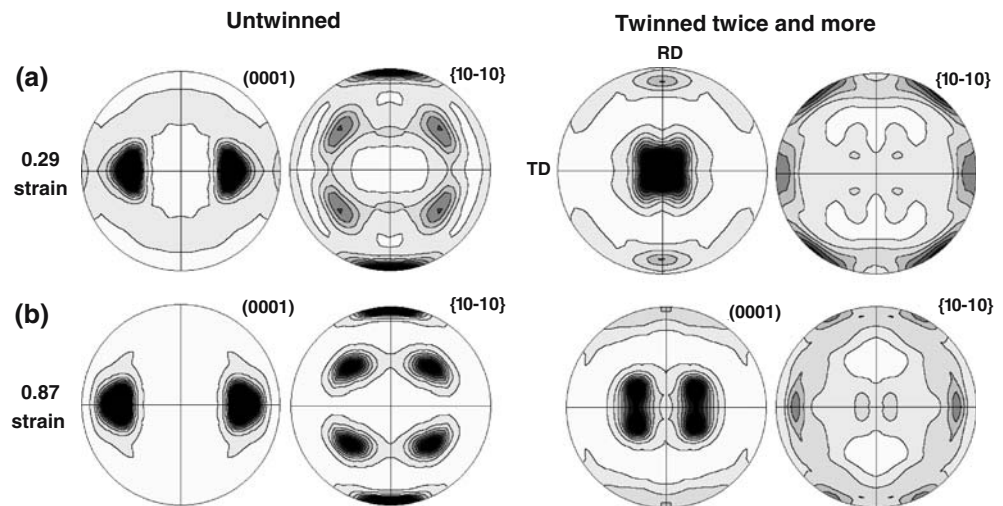


Twinning seems to be a crucial factor in determining the local deformation structure. It was also an important ingredient in getting simulated texture components to match the experimental ones. Hardening laws were chosen to increase hardening on twin systems relative to slip systems and give slip a preference over twinning in the later stages of deformation. Also the total twinned volume was limited. Even so many grains underwent multiple twinning. We have sorted all 2000 orientations according to the number of times a grain has undergone twinning (Fig. 9). The orientation of the untwinned grains after 0.87 as well as after 0.29 strain defines a single component with a [0001] maximum at 50° inclined towards the transverse direction and a strong {10-10} maximum in the rolling direction, i.e. centered on $\{\varphi_1 = 0^\circ, \Phi = 50^\circ, \varphi_2 = 0^\circ\}$. By contrast,

the multiply twinned grains (twice and more) have a strong [0001] maximum in the normal direction after 0.29 strain. This maximum splits into two peaks tilted towards $\pm\text{TD}$ after 0.87 strain. The corresponding {10-10} poles are in a broad girdle distribution with no maximum near the rolling direction. This reflects the behavior of the experimentally observed C component which appears at $\{\varphi_1 = 0^\circ, \Phi = 0^\circ, \varphi_2 = 30^\circ\}$ for intermediate strains and disappears again for higher strains. The orientations of the multiply twinned grains present a secondary distribution characterized by (0001) poles perpendicular to the normal direction, with a concentration near the rolling direction.

To better understand the effect of twinning, the rotation trajectories of individual grains will now be analyzed. Figure 10 shows the behavior of four different

Fig. 9 Orientation of untwinned grains and multiply twinned grains displayed on $\{0001\}$ and $\{10\text{--}10\}$ pole figures (equal area projections). (a) 0.29, (b) 0.87 effective strain



initial orientations. This figure shows how these orientations transform at each of the 30 steps of 0.029 strain considered in the simulation. The model does not allow grain fragmentation but makes a complete grain either completely twin/rotate or not at each step. By contrast in the real microstructure twinning and slip cause fragmentation. The individual rotation trajectories will be interpreted here as the set of the orientations which can be produced from an initial one.

Figure 10a shows that the orientations $\{\varphi_1 = 0^\circ, \Phi = 40^\circ, \varphi_2 = 0^\circ\}$ are very stable. The corresponding grains deform on two prismatic systems without resulting rotation, except a slight tilt of the $[0001]$ axis towards \pm TD. These orientations belong to the main texture component after 80% cold-rolling (component A). With identical initial $[0001]$ axis position but a 30° rotation of $\langle 10\text{--}10 \rangle$ axes (i.e. $\{\varphi_1 = 0^\circ, \Phi = 40^\circ, \varphi_2 = 30^\circ\}$, Fig. 10b), deformation causes a rotation of $\langle 10\text{--}10 \rangle$ around the $[0001]$ axis towards RD. This is done with activity on two prismatic systems, but different ones compared to the previous case so that the combination of the two slip systems induce a rotation of the grains. Grains oriented at $\{\varphi_1 = 0^\circ, \Phi = 50^\circ, \varphi_2 = 0^\circ\}$ and $\{\varphi_1 = 0^\circ, \Phi = 50^\circ, \varphi_2 = 30^\circ\}$ do behave similarly as the previous ones, respectively. The grains with $[0001]$ axes tilted by $40\text{--}50^\circ$ from the normal direction to the transverse direction do not twin (Fig. 9). This is in full agreement with the experimental results. The position of the $[0001]$ axes in the lamellar structures is indeed usually close to the TD–ND plane and about 50° away from ND.

The grains which twin have either $[0001]$ axes at low ($<30^\circ$) or high ($>70^\circ$) angles to ND. The related rotation trajectories are shown on Fig. 10c and d respectively. Orientations with $[0001]$ axes close to the

normal direction (Fig. 10c) are favorably oriented for compressional twinning. Those at high Φ angles (Fig. 10d) have high shears on prismatic systems and, in addition, twin by tensile twinning at larger strains. Among all the orientations with high Φ angles, the ones in the $\varphi_1 = 0^\circ$ section (experimental D component) are not, according to the model, optimal for tensile twinning. This might be the reason why they do not disappear again as component C does. Nevertheless, as a general rule, after compressional twinning, orientations are in good orientations for tensile twinning and, if multiple twinning is allowed, twinning may repeat. This may be an effective mechanism in producing a fine-grained microstructure. In addition, these individual rotation trajectories show how wide the orientation spread produced by twinning can be. In particular, the secondary texture components observed in the $\varphi_1 = 0^\circ$ ODF section at $\{\Phi = 0^\circ, \varphi_2 = 30^\circ\}$ and $\{\Phi = 90^\circ, \varphi_2 = 0^\circ\}$ which develop at intermediate strains (Fig. 1) are closely related to twinning. They are both produced by twinning (Figs. 4b and 9). The C component is well oriented for compressive twinning and it disappears for high strains, D component is not favorably oriented for tensile twinning and it remains until 80% thickness reduction. In addition to “randomizing” the texture in the first stages of cold-rolling, twinning and especially multiple twinning may also play an important role in the subsequent disappearance of some texture components.

In a previous paper, the recrystallization behavior of this material was described [12].

Recrystallization proceeds in two steps, one extremely fast concerning 85 vol.% of the material, and a much slower one for the remaining 15 vol.%. The complete recrystallization is reached after 4 h at

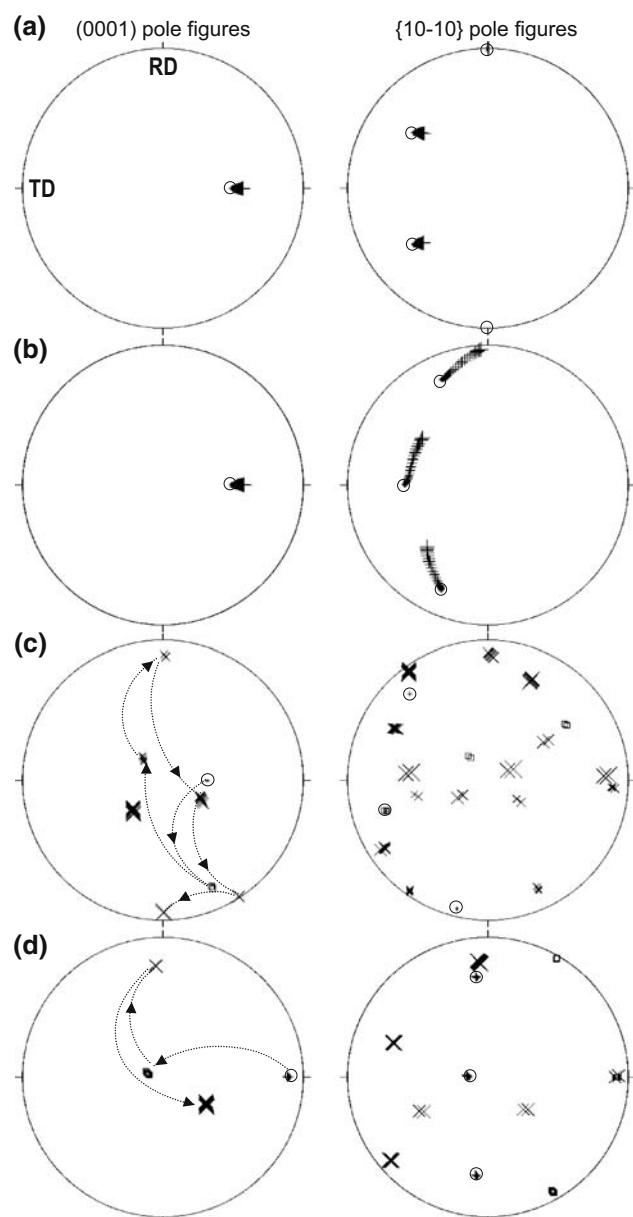


Fig. 10. Individual rotation trajectories for grains of different initial orientations: (a) $\{\varphi_1 = 0^\circ; \Phi = 40^\circ; \varphi_2 = 0^\circ\}$, (b) $\{\varphi_1 = 0^\circ; \Phi = 40^\circ; \varphi_2 = 30^\circ\}$, (c) $\{\varphi_1 = 0^\circ; \Phi = 25^\circ; \varphi_2 = 45^\circ\}$, (d) $\{\varphi_1 = 0^\circ; \Phi = 80^\circ; \varphi_2 = 30^\circ\}$. Equal area projections. Symbols: \circ = initial position; $+$ = has not twinned; \square = twinned once; \times = twinned more than once. Symbol size increasing with strain

500 °C but 85 vol.% have already recrystallized during the first 40 min. This striking kinetic difference is clearly related to the deformation structures and to the deformation mechanisms active in the two parts of the material. In the 85 vol.% of the material which have undergone twinning and show a very fine subdivided structure with high misorientations after 80% cold-rolling, the recrystallization driving force is extremely

high and the recrystallization proceeds very fast. Shear bands were not identified as preferential recrystallization sites, which is consistent with the present results. The fragmentation scale in the rest of the 85 vol.% and the orientation scattering of the fragments seem to be similar as they are in the shear bands. Therefore the recrystallization driving force is similar everywhere in the fine-subdivided part and the shear bands do not behave specifically with regards to the recrystallization mechanisms and kinetics.

By contrast, the lamellar structures produced by slip in the grains which do not twin, exhibit a much lower driving force for recrystallization because the size of the cells is much larger and the local misorientations very low. These areas recrystallized by extended recovery or by being consumed by neighboring grains, both mechanisms being quite slow.

Conclusions

In this study we combined conventional texture analysis, using X-ray pole figures, with a microstructural orientation investigation. We could establish a close link between microstructural features in the deformed state and initial grain orientation. For the interpretation it was helpful to use polycrystal plasticity simulations not so much to assess bulk textures, but to explore the behavior of individual grains. The rotation trajectories of individual orientations showed striking similarities with the orientations measured locally in few- μm^2 wide areas in the deformed samples. These trajectories were interpreted as the sets of orientations which can be produced from a given initial orientation.

The 80% cold-rolled microstructure of commercially pure titanium is extremely heterogeneous. About 85 vol.% of the material, including shear bands, is very fine subdivided and presents high misorientations even at the sub-micrometer scale. This part of the material has undergone twinning during deformation. Multiple twinning is an effective mechanism of grain fragmentation in the beginning of deformation. The twins are further deformed and fragmented into increasingly smaller domains by slip system activity. This part of the material has a high driving force for recrystallization and recrystallizes indeed very fast. The other 15% of the material correspond to the grains which are not favorably oriented for twinning. In these grains, only slip systems are active and produce lamellar structures. The combined use of high-resolution EBSD mapping and local orientation measurement in the TEM provides with a very detailed idea of

the orientation gradients inside the lamellae. For example, the orientation gradually changes along the rolling direction, with keeping the [0001] axis in constant position and $\langle 10\bar{1}0 \rangle$ rotating around it. This fits very well with the simulation results for grains deforming by slip on prismatic systems. The cumulative misorientation throughout the lamellae can comprise several tens of degree but the local misorientations, in the micrometer range, are very low. This provides a much lower driving force for recrystallization and therefore a much lower recrystallization speed.

References

- Kelly EW, Hosford WF (1968) *Trans TMS-AIME* 242:654
- Mcdarmid DS, Partridge PG (1986) *J Mater Sci* 21:1525
- Partridge PG (1957) *Metall Rev* 118:169
- Fundenberger JJ, Philippe MJ, Wagner F, Esling C. (1997) *Acta Mater* 45:4041
- Zaefferer S (2003) *Mater Sci Eng A* 344:20
- Philippe MJ, Serghat M, Esling C, Van-Houtte P (1995) *Acta Metall Mater* 43:1619
- Prantil VC, Jenkins JT, Dawson PR (1995) *J Mech Phys Solids* 43:1283
- Lenbensohn RA, Tomé CN (1993) *Acta Metall Mater* 41:2611
- Grewen J (1975) In: *Proceedings of the 3rd European texture conference*, Société Française de Métallurgie (ed), Paris, p 195
- Inoue H, Inakazu N (1988) In: Kallend JS, Gottstein, G (eds) *Proceedings of 8th international conference on textures of materials*. The Metallurgical Society Inc., Warrendale, PA, p 997
- Singh AK, Schwarzer RA (2000) *Z Metallkd* 91:702
- Wagner F, Bozzolo N, Van Landuyt O, Grosdidier T (2002) *Acta Mater* 50:1245
- Puig-Molina, Wenk HR, Berberich F, Graafsma H (2003) *Z Metallkd* 94:1199
- Dahms M, Bunge HJ (1989) *J Appl Cryst* 22:439
- Wagner F, Dahms M (1991) In: Bunge HJ, Esling C (eds) *Advances and applications of quantitative texture analysis*. DGM Oberursel, p 101
- Fundenberger JJ, Morawiec A, Bouzy E, Lecomte JS (2003) *Ultramicroscopy* 96:127
- Bunge HJ (1982) *Texture analysis in material science*. Butterworths, London
- Molinari A, Canova GR, Ahzi S (1987) *Acta Metall* 35:2983
- Lebensohn RA, Tome C (1993) *Acta Mater* 41:2611
- Tomé CN, Lebensohn RA, Kocks UF (1991) *Acta Metall Mater* 39:2667
- Lebensohn RA, Sanchez PV, Pochettino AA (1994) *Scripta Metall Mater* 30:481
- Lebensohn RA, Tomé CN, Wenk HR (1994) *Mater Sci Eng A* 175:71
- Lebensohn RA, Gonzalez MI, Tomé CN, Pochettino AA (1996) *J Nucl Mater* 229:57
- Van-Houtte P (1978) *Acta Metall* 26:591
- Bozzolo N, Dewobroto N, Grosdidier T, Wagner F (2005) *Mater Sci Eng A* 397:346
- Nauer-Gerhardt CU, Bunge HJ (1988) In: Kallend JS, Gottstein G (eds) *Proceedings of 8th international conference on textures of materials*. The Metallurgical Society Inc., Warrendale, PA, p 505
- Van Landuyt O, Grosdidier T, Wagner F (1999) In: Szpunar JA (ed) *Proceedings of the 12th international conference on texture of materials*. NRC Research Press, Montréal, p 895